ELSEVIER

EXTREME MECHANICS LETTERS

Volume 48 October 2021 ISSN 2352-4316

COVER IMAGE

Uniaxial stretch-release of rubber-plastic bilayers: Strain dependent transition to stable helices, rolls, saddles, and tube

Extreme Mechanics Letters 48 (2021) 101384

Contents lists available at ScienceDirect

Extreme Mechanics Letters

journal homepage: www.elsevier.com/locate/eml

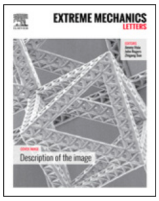

Uniaxial stretch-release of rubber-plastic bilayers: Strain-dependent transition to stable helices, rolls, saddles, and tubes

Rahul G. Ramachandran [a], Jonah de Cortie [a], Spandan Maiti [b,a,c,d], Luca Deseri [e,a,f,g,h], Sachin S. Velankar [c,a,d,*]

[a] Department of Mechanical Engineering and Materials Science, University of Pittsburgh, Pittsburgh, PA, United States
[b] Department of Bioengineering, University of Pittsburgh, Pittsburgh, PA, United States
[c] Department of Chemical Engineering, University of Pittsburgh, Pittsburgh, PA, United States
[d] McGowan Institute for Regenerative Medicine, University of Pittsburgh, Pittsburgh, PA, United States
[e] Department of Civil, Environmental and Mechanical Engineering, University of Trento, Trento, Italy
[f] Department of Mechanical Engineering, Carnegie Mellon University, Pittsburgh PA, United States
[g] Department of Civil and Environmental Engineering, Carnegie Mellon University, Pittsburgh PA, United States
[h] Department of Nanomedicine, The Methodist Hospital Research Institute, Houston TX, United States

ARTICLE INFO

Article history:
Received 29 January 2021
Received in revised form 26 May 2021
Accepted 5 June 2021
Available online 10 June 2021

Keywords:
Bilayer
Plasticity
Composites
Shape change
Strain mismatch
Wrinkling

ABSTRACT

Polymeric plastics deform irreversibly (i.e., inelastically) whereas rubbers deform reversibly, i.e., elastically. Thus, uniaxially stretching a rubber-plastic bilayer composite beyond its yield point can create an elastic strain mismatch between the two layers. Upon release, the bilayer may then bend out-of-plane. We quantify the mechanics of such stretch-release-induced shape changes in rectangular specimens of rubber-plastic bilayers. We show a remarkable dependence of the final shape upon the stretch applied prior to release. At small stretch, all bilayers bend into arch or roll shapes with the plastic on the convex face. At large stretch, the bilayers bend into half-tubes with the plastic, now heavily-wrinkled, becoming the concave face. Thus, the sign and direction of the curvature both flip as applied stretch increases. Between these two extremes, saddle shapes appear which have characteristics of both arches as well as half-tubes. Sufficiently narrow samples show different behavior: they transition from arches to helices as stretch increases. All these shapes are mono-stable. We document numerous ways in which the mechanics of rubber-plastic bilayers differs from that of fully-elastic bilayers. Most importantly, yielding of the plastic layer during the shape change strongly affects the mechanics of the elastic–plastic bilayers, and yielding accompanied by plastic wrinkling has an especially large effect. A strain energy model illustrates how the shape change is dictated by the change in the ratio of elastic strain mismatch in the two directions due to the formation of wrinkles at the rubber-plastic interface.

1. Introduction

When stretched, an elastomeric sheet stores the work done on it as elastic energy and recovers its original shape upon unloading. In contrast, a sheet of yielding material dissipates almost all the work of stretching, and therefore remains at or near its stretched configuration when unloaded. A composite bilayer composed of these two materials, when stretched and unloaded, can bend out-of-plane, sometimes with interfacial buckling or wrinkling. This article is about the various mono-stable shapes with single or dual curvature formed by a uniaxial stretch and release of a rubber-plastic bilayer. The central focus of this article is to elucidate the role of inelastic deformation in the bending process.

Elastic strain mismatch within a material can trigger complex shape deformations. Hence it is a powerful tool for creating intricate shapes and structures. In nature, plants and animal tissues exploit growth-induced heterogeneous elastic strain to create a myriad of static shapes and dynamic mechanisms. Opening of seed pods by elastic incompatibility [1], growing complex three dimensional features in internal organs [2,3], twisting of plant tendrils [4], curvatures in leaves [5] and others [6–8] are all examples of shape changes through inhomogeneous strain generation. Many researchers have sought to exploit such shape changes for engineering [9–11] and biomedical [2,12,13] applications. Heterogeneous strain driven fabrication techniques have also found popularity in micro- and nano-scale fabrication [12,14–16], where it

---

[*] Corresponding author at: Department of Chemical Engineering, University of Pittsburgh, Pittsburgh, PA, United States.
E-mail address: velankar@pitt.edu (S.S. Velankar).

https://doi.org/10.1016/j.eml.2021.101384

is difficult to create intricate 3D shapes with conventional methods. Nano tubes and channels and many other three-dimensional shapes can be created through these techniques. Morphology changes driven by controllable strain gradients are also explored widely in the literature [17–21].

Much previous research on shape changes has created a strain mismatch by applying a uniform stimulus to a heterogeneous structure. A common example of this mechanism is the bimetallic strip sometimes used in household thermostats. A bimetallic strip is made by bonding two metals with unequal thermal expansion coefficient. When heated, the strip bends into an arch, with the metal with higher thermal expansion coefficient material on the outside. Instead of thermal expansion, other stimuli such as differences in solvent swelling of the layers [16,22–24], or shape memory of one of the layers [25], can also be used to induce bending. The rest of this paper focuses on such bilayers in which a large difference in mechanical properties between layers induces shape changes.

Some of the recent fundamental research on bilayer mechanics was conducted by bonding together layers while holding one or both layers prestretched [18,26–28]. Upon bonding the layers and then releasing, the composite specimen adopted a bent configuration. When the prestretched layer was under equi-biaxial stretch, the composite bilayers bent into bistable cylinders or spherical bowls depending on thickness and width of the specimen as well as the applied prestretch [26]. Unlike a bimetallic strip where the strain mismatch is inherently isotropic, prestretching allows investigations of anisotropic strain states. In [26] it is found that the curvatures of the system bifurcate upon reducing bilayer thickness, and such bifurcation separates two scaling regimes for the energy of the system. In a related work, upon searching for isometries from a reference surface of the bilayer, DeSimone modeled the effects of bonding a uniaxially prestretched rubber layer to an unstretched rubber layer [27]. This is done in [27] using a novel finite dimensional constrained energy minimization problem. Upon unloading, the composite bilayer bent into an mono-stable roll, with the prestretched layer on the inside [27]. In contrast, Chen et al. bonded rubber layers that were both prestretched, but along perpendicular directions [29]. Upon releasing, the composite bilayers bent into saddle shapes or bistable cylinders depending on thickness and width of the specimens [29]. Such bonding with prestretch also allows investigations of how specimen geometry couples with anisotropy in prestretch, e.g. a rectangular strip where the long direction is at an angle with respect to the prestretch direction forms a helical shape [27].

This article focuses on shape changes occurring due to a *deformation-induced strain mismatch*. Specifically, we examine shape changes of a rubber-plastic bilayer which has been uniaxially stretched, and then released, as illustrated in Fig. 1B. First consider the free-standing layers of the rubber and the plastic, Fig. 1A. Upon stretch-release, the rubber layer recovers its original configuration, whereas the plastic maintains its stretched shape. Now consider a bilayer in which these two layers are bonded to each other, both under stress-free conditions. Upon stretching, an elastic strain mismatch is created. Thus, upon releasing, the bilayer is expected to bend (Fig. 1B).

Real rubbery materials are not perfectly elastic and may undergo modest inelastic deformations. Similarly, real plastics do not maintain their deformed shape perfectly, but instead show modest shape recovery after deformation. Nevertheless, provided that the degree of inelastic deformation of the two layers is unequal, bending is expected. Excellent examples of such bending are shown by Wisinger et al. [30]. Incidentally note that Fig. 1, which is a 2-dimensional illustration, only shows simple arch shapes, whereas Wisinger et al. showed arches as well as helical shapes, depending on the magnitude of elastic strain mismatch. This paper will show an even wider range of complexity including the saddle shapes mentioned in the previous paragraph for fully elastic bilayers. Further, we will show that even the direction and sign of the curvature depend on the applied stretch, a complexity not reflected in Fig. 1.

The *deformation-induced strain mismatch* of Fig. 1B is a powerful means to realize shape-morphing materials. Changes in shape can be induced by simply stretching the material to the desired extent, instead of stimuli such as light or heat [28,30]. Irreversible deformation is common amongst a variety of materials including metals, polymers, or even amorphous particulate materials, and hence this approach can be applied to a variety of systems. Indeed, an excellent example is of helically-coiled synthetic muscle fibers which were created by simply stretching an elastic–plastic composite [13].

Despite the potential power of elastic–plastic composites to realize complex shape changes, their mechanics is poorly understood, even for the case of bilayers. At first glance, it is tempting to interpret such bending as being analogous to the shape change of an elastic–elastic bilayer with a strain mismatch. This analogy is illustrated in Fig. 1C: the stretched state of the elastic–plastic bilayer is regarded as equivalent to bonding a stress-free elastic layer to a rubber layer pre-stretched to the same dimensions [30]. As per this analogy, the *only* role of inelastic deformation is to create a strain mismatch when the sample is stretched; the mechanics after release presumes that both materials behave elastically. Indeed, this "elastic-after-release" is exactly the modeling approach followed by Wisinger et al. [30]. Yet, although the analogy of Fig. 1C is useful, inelastic deformation may have several consequences beyond merely creating the strain mismatch upon stretching.

First, upon releasing, the plastic layer experiences compression, and if the compressive stress exceeds the yield stress of the plastic, it will deform inelastically. Fig. 1B presumes that the plastic remains at its stretched dimensions upon release, but if it yields in compression, the degree of bending will reduce. This is well-recognized in bimetallic strips in which, if the yield stress of one of the layers is exceeded, the curvature becomes much less sensitive to temperature changes [31,32]. An example will be shown in this paper.

Second, if the elastic layer is relatively soft and thick, the plastic face of the bilayer may buckle in compression and develop wrinkles at sufficiently large strain mismatch [33–36]. In fact, wrinkles may develop even for a purely elastic bilayer in the geometry of Fig. 1C [37–43], but in elastic–plastic composites, the wrinkling is coupled with yielding, and wrinkles can form before or after yielding [36]. This paper will show that yielding occurs before wrinkling, and wrinkles persist even when the plastic layer is debonded from the rubber, which indicates the formation of plastic hinges. The effect of wrinkles on shape changes have not been explored in this context before.

Third, in fully-elastic bilayers, bistable shapes are encountered commonly. Bistability can be desirable, e.g. Venus flytrap relies on the snap-through of a double curvature surface [44] or snapping mechanical wires [45] and many others reviewed in [46]. Similarly, a biaxial elastic strain mismatch can induce bistability such that the bilayer can bend in one of two possible directions [26,27]. However, bistability may not be desirable and considerable research been done on guiding the direction along which curvature develops [25,47,48]. This article shows that rubber-plastic bilayers tend to form single stable shapes. Thus, no external control other than the magnitude of applied stretch is required to control the final morphology.

Finally, even during the stretching process itself, inelastic deformation may introduce complexities beyond merely introducing a strain mismatch. Free-standing plastic layers are prone to

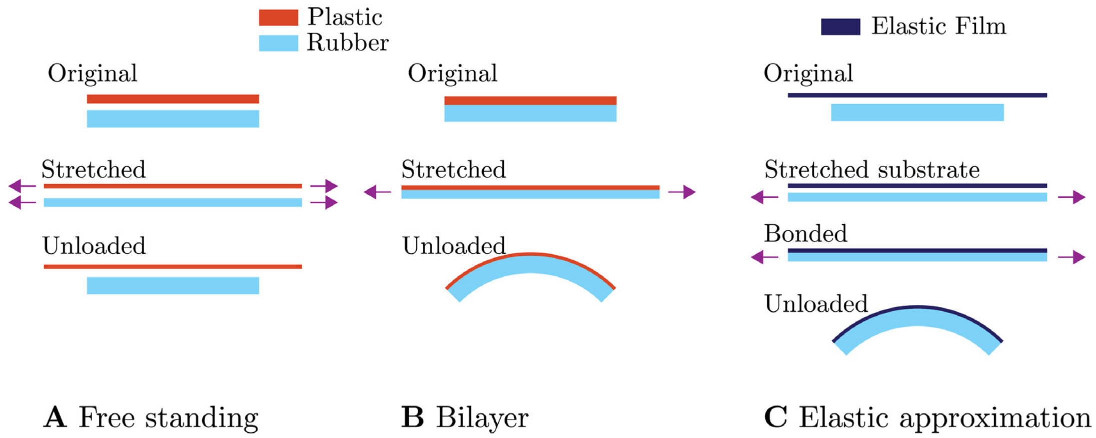

Fig. 1. Schematic of rubber and plastic behavior when stretched and unloaded. (A) Both the layers are free-standing. (B) The layers are bonded, forcing equal deformation at the interface. (C) Schematic of shape change that occurs when a stretched rubber substrate is bonded to an unstretched elastic film, and then released.

necking behavior in tension, and free-standing polymeric plastic layers may also show stable neck propagation [49]. Bonding an elastic layer to a plastic reduces the tendency for necking, nevertheless, if the elastic layer is sufficiently thin or soft, an elastic–plastic bilayer may show necking and/or stable neck propagation [50–55]. Thus, due to non-homogeneous stretching, inplane strain gradients may develop during the stretching phase, which would then affect subsequent shape changes. An example of this will also be shown in this paper.

In summary, the above arguments suggest that an "elastic-after-release" framework is tenable only if (1) the elastic–plastic bilayer deforms homogeneously during stretching, (2) compressive stress developed in the plastic layer after release is lower than its yield stress and (3) surface instabilities like wrinkles do not appear. The second and third condition suggests that elastic strain mismatch must depend, even qualitatively, on the applied stretch. Upon releasing from a low stretch, the rubber imposes only a modest compressive stress on the plastic layer, and hence the plastic may not yield. However, upon releasing after a large applied stretch, the rubber must impose a correspondingly large stress on the plastic, and yielding and wrinkling become likely. Indeed, this paper confirms a significant dependence of shape changes on the applied stretch.

This article is organized as follows. Section 2 describes the materials and methods, including a list of symbols in Table 1. Section 3.1 describes experimental observations of rubber-plastic bilayers subjected to stretch and release. We show that even the qualitative nature of shape changes in such composites depend on the applied strain. Sections 3.2 and 3.3 show how the sample geometry affects the results, in particular that narrow specimens are susceptible to twisting deformations. Finally, Section 3.4 shows non-homogeneous bending that occurs because the plastic layer is prone to necking. An analytical model is described in Section 4 which shows how modification in elastic strain mismatch due to inelastic deformation and wrinkling during release can lead to flip in sign and direction of the curvature with increasing stretch. Section 5 summarizes the paper.

2. Methods

2.1. Experimental

Sheets of natural rubber (McMaster Carr) of undeformed thickness, $H^r = 250\ \mu$m, 500 μm and 750 μm were used as the elastomer layer. Sheets of linear low-density polyethylene (LLDPE) of $H^p = 50\ \mu$m thickness was used as the plastic. Rubber-plastic bilayers of different thickness ratios were prepared by bonding the LLDPE sheets to the rubber sheets. The bond was made by passing the two layers together through heated mechanical rollers to eliminate air pockets, and then heating to 150°C and holding for 10 mins to strengthen the bond. Rectangular specimens of 22 mm length and various width from 2 mm to 16 mm were then cut out using punches. The test specimens were stretched and unloaded on an MTS® tensile testing machine at a clamp speed of 5 mm/min. Either ink marks or small particles were applied on the rubber side of the samples, the tests were video-recorded, and the marker displacements were calculated by Digital Image Correlation (DIC) analysis using the Blender software. The true stretch along the X-direction (λ_x) was then calculated from the marker displacements as described in our previous publication [50]. Only regions of the samples away from the grips were used in this analysis. These true values of λ_x measured directly from the images were typically somewhat smaller than nominal values expected from the motion of the clamps. This may be due to slipping of the specimen at the grips at large stretches, or slightly non-homogeneous deformation near the sample ends. We will only use true values throughout this paper. The highest value of λ_x for any given specimen, designated λ_{max}, is used as a measure of imposed stretch.

To study the effect of applied stretch on the final morphology, each sample was stretched to the desired extent, corresponding to λ_{max} values ranging from 1.4 to 3.8, and then unloaded. The end-sections of the samples that had been clamped in the tensile testing device were then cut off with a razor blade, thus leaving only the sections that had experienced stretching. These final equilibrium shapes were photographed.

The stress-free state of the layers in the bilayer after deformation was studied by forcing delamination of the layers. Partial or full delamination happened naturally after several days' storage. Partially delaminated samples were then exposed to solvent heptane to achieve complete delamination.

The experiments of Section 3.5, on samples that show necking in tension, used a different pair of materials that will be described in that section.

2.2. Material behavior

Prior to measuring the behavior of the free-standing monolayers, LLDPE and rubber samples were first heated identically as the bilayers to erase any possible processing effects from the film manufacturing. Figs. 2A and 2C show the Cauchy stress (σ)

Table 1
List of symbols used in this paper.

H^r, H^p	Thickness of rubber layer and plastic layer in the undeformed configuration
h^r, h^p	Thickness of rubber layer and plastic layer in the deformed configuration
λ_x, λ_y	Stretch along the X and Y-direction away from the grips
λ_{max}	Highest value of λ_x imposed during the stretching
σ	Cauchy stress
λ^p_{per}, λ^r_{per}, λ_{per}	Permanent stretch in the plastic, rubber, and bilayer after unloading from a stretch of λ_{max}
$\lambda_{x,mis}$, $\lambda_{y,mis}$	Stretch mismatch in the X and Y-directions estimated from free-standing rubber and plastic layers
$\bar{\lambda}_{x,mis}$, $\bar{\lambda}_{y,mis}$	Effective stretch mismatch in the X and Y-directions estimated from the bilayer experiments
κ_y	Curvature in the XZ plane with normal along Y-direction
κ_x	Curvature in the YZ plane with normal along X-direction
ψ^r	Strain energy density function of the rubber
V^r	Volume of rubber layer
U^r	Total strain energy in the rubber layer

vs true stretch in the X-direction (λ_x) response of LLDPE and the rubber films after stretching to three different values of stretch. The Cauchy stress was computed as $\sigma = \frac{F}{A_o}\lambda_x$ where F is the reaction force measured and A_o is the original cross section area of the specimens.

In all cases, the force increased during stretching, and then decreased back to zero during release. The stretch, λ_x at which the force reverted to zero during release is dubbed the "permanent stretch" (λ_{per}) and is a measure of inelastic deformation. The LLDPE underwent significant permanent deformation after stretching, e.g., after stretching to $\lambda_{max} = 3.8$ and then releasing, the sample recoiled to a permanent stretch of $\lambda^p_{per} = 2.98$. The permanent stretch in plastic (λ^p_{per}) obtained from three experiments in Fig. 2A is plotted against the λ_{max} in Fig. 2B, along with a straight line fit:

$$\lambda^p_{per} = 0.84\lambda_{max} - 0.25 \tag{1}$$

Eq. (1) does not have physical significance but will only be used to interpolate between the experimentally recorded λ_{max} values in the range $1.8 < \lambda_{max} < 3.8$.

In contrast to the plastic, the rubber is much more elastic, e.g., after releasing from a λ_{max} of 3.3, the rubber recoils to a permanent stretch of $\lambda^r_{per} \approx 1.08$, indicating only a small permanent deformation. It is this difference between the degree of elastic recoil that causes the strain mismatch, which in turn induces shape changes.

Since λ^r_{per} is close to 1 (i.e., the rubber recovers almost completely), the stretch mismatch between the free-standing layers is taken as equal to the permanent stretch in the plastic layer ($\lambda_{x,mis} = \lambda^p_{per}$). It is this mismatch stretch that induces severe bending. Note that if the layers follow uniaxial deformation kinematics with $\lambda_y = 1/\sqrt{\lambda_x}$, there must be a strain mismatch in the Y-direction with magnitude $\lambda_{y,mis} = 1/\sqrt{\lambda_{x,mis}} = 1/\sqrt{\lambda^p_{per}}$. The two mismatch stretches are shown in Fig. 11A, to be discussed later.

Incidentally, it is noteworthy that for the plastic, a plot of force vs stretch (or equivalently engineering stress, F/A_o vs stretch, dashed curve shown in ESI Fig. S2) does not show a peak; such a peak would indicate necking. Moreover, quantitative video analysis confirms that LLDPE stretches uniformly. This is in contrast to the necking seen in many semi-crystalline polymers. The engineering stress vs stretch of such a necking material is also presented in ESI Fig. S2 (purple curve). Section 3.5 will show an example of such a necking plastic.

3. Results

The schematics of stretch-release and subsequent morphology change is shown in Fig. 3A. The initial sample dimensions are denoted L, W, and H along the X, Y, and Z directions respectively. When a stretch λ_x is applied, the length increases but the width, w and thickness, h in the stretched configuration both reduce due to the Poisson effect.

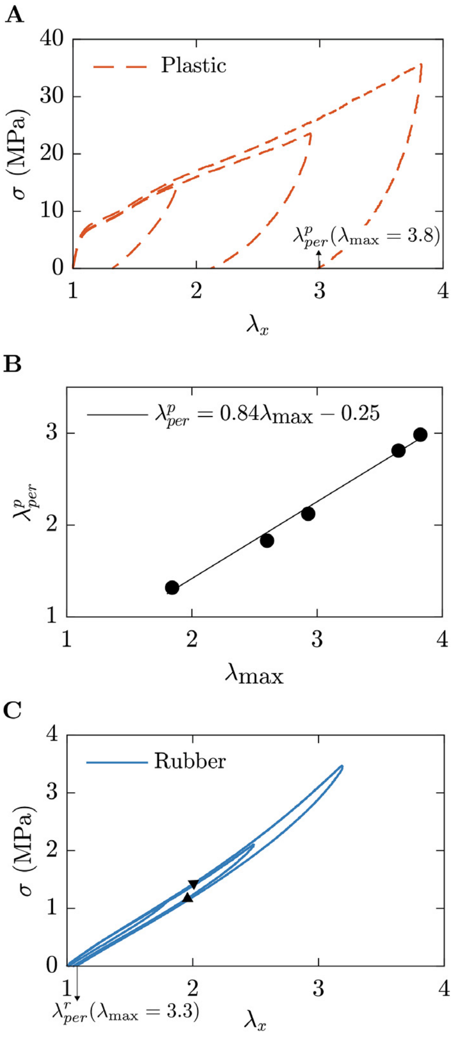

Fig. 2. (A) Cauchy stress (σ) vs true stretch in the X-direction (λ_x) for LLDPE film. The permanent stretch (λ^p_{per}) is marked for the curve with $\lambda_{max} = 3.8$ (B) λ^p_{per} for the three curves in Fig. 2A vs corresponding λ_{max}. (C) σ vs λ_x for natural rubber.

The final morphology after unloading can have two curvatures. The curvature about the Y-axis (i.e., in the XZ plane) is marked as

κ_y, whereas the curvature about the X-axis (i.e., in the YZ plane) is denoted as κ_x. In some cases, one of these curvatures may be nearly zero.

3.1. Roll to half-tube transition with increasing λ_{max}

As mentioned in Section 2.2, the strain mismatch between the rubber and plastic layers increases with increasing λ_{max}. Accordingly, the shapes after stretch-release also depend on the λ_{max}, as shown in Fig. 3B–I. These figures all correspond to rectangular bilayer specimens of initial dimensions $L = 18\,\text{mm}$ and $W = 8\,\text{mm}$, released after various applied stretches. The rubber and plastic had a thickness of $H^r = 750\ \mu\text{m}$ and $H^p = 50\ \mu\text{m}$ respectively. Only the applied stretch was varied. At the lowest λ_{max} value of 1.4, the sample bends into an arch shape with the plastic layer being on the outside of the arch, i.e., $\kappa_y > 0$ and κ_x is nearly zero (in fact, slightly negative). With increasing λ_{max}, κ_y increases significantly as the sample forms a roll shape, but κ_x remains near zero. Once the $\lambda_{max} \geq 2.9$ (Fig. 3F), the samples adopt a saddle-shape, i.e., dual curvature with $\kappa_y > 0$ and $\kappa_x < 0$. It is noteworthy that κ_y now reduces with increasing stretch. With further increase in λ_{max}, κ_y continues reducing whereas κ_x becomes increasingly negative, i.e., the samples gradually revert to having a mono-curvature, but with a sign and direction that both are flipped with respect to the original arch. The shape of Fig. 3J is dubbed a "half-tube" in this paper. A final interesting feature is that for $\lambda_{max} \geq 2.8$, wrinkles appear. These wrinkles are always oriented parallel to the width direction and are always on the plastic face of the specimens.

The curvature values, κ_x and κ_y quantified by image analysis (see Fig. S1 in supplementary material) for the specimens of Fig. 3B–I are shown in Fig. 3J. This figure clearly shows the non-monotonic nature of κ_y. Further, the maximum in κ_y also roughly coincides with the stretch at which κ_x first deviates significantly from zero.

3.1.1. Inelasticity in compression and wrinkling of film

A key question raised in the Introduction is: to what extent is the deformation inelastic during the release process? We address this question by debonding the layers after stretch release and letting them revert to their stress-free shapes. These debonded layers can then be compared with free-standing layers stretched to the same extent. If the permanent deformations of these debonded layers agree with those expected for the free-standing layers (permanent stretch of the plastic layer should be λ^p_{per} from Fig. 2B, and permanent stretch of the rubber layer should be nearly 1), an elastic-upon-release view would be justified. Any deviation would indicate inelastic deformation during the release.

Two examples are shown in Fig. 4. Fig. 4A corresponds to an 18 mm × 12 mm sample ($H^r = 750\ \mu\text{m}$) with $\lambda_{max} = 2.8$, for which the shape prior to debonding was a roll with $\kappa_y > 0$ and $\kappa_x \approx 0$. The shape is not a perfect cylinder but shows a small gradient in curvature. Upon debonding, the plastic film remained in the form of a roll (Fig. 4A) with little apparent change as compared to the fully bonded bilayer. Meanwhile the rubber recovered its undeformed shape almost completely. The roll-shaped plastic layer was then gently unrolled, placed alongside the corresponding delaminated rubber, and held flat by placing it under a thin acrylic sheet. This image of the two layers side-by-side is also included in Fig. 4A. It is immediately apparent that the debonded plastic layer is only about 10% longer than the rubber layer (i.e., its permanent stretch is only 1.1), indicating only a small elastic mismatch. Moreover, substituting $\lambda_{max} = 2.8$ into Eq. (1) gives $\lambda^p_{per} = 2.1$, i.e., the free-standing plastic, released from the same stretch, would end up almost twice as long as the debonded plastic from Fig. 4A. This is clear evidence that the rubber was able to inelastically compress the plastic layer significantly, almost back to the stress-free configuration of the rubber itself.

Fig. 4B corresponds to a sample with applied $\lambda_{max} = 3.1$, where the shape prior to release (Fig. 3I) is nearly a half-tube with $\kappa_x < 0$ and $\kappa_y = 0.04\,\text{mm}^{-1}$ with wrinkles on the plastic face. The λ_{per} of the half-tube was measured to be nearly 1, i.e., the rubber nearly recovered its undeformed length even prior to debonding. The plastic layer accommodated this by wrinkling and/or in-plane yielding. Upon debonding, the plastic layer remained permanently wrinkled, whereas faint lines are apparent in the rubber that indicate some local damage at the wrinkle locations. An image of the two delaminated layers flattened by weighing down with an acrylic sheet is also included in Fig. 4B. Unlike Fig. 4A, there is now a large mismatch in length and width of the two debonded layers. The end-to-end length of the flattened delaminated plastic in Fig. 4B is found to be 1.5 times of the delaminated rubber. In fact, the wrinkles on the delaminated plastic are not perfectly flattened by the acrylic sheet, and hence its true contour length is somewhat larger. Nevertheless, the contour length is significantly less than would be expected for free-standing plastic ($\lambda^p_{per} = 2.35$, obtained by substituting $\lambda_{max} = 3.1$ into Eq. (1)). Thus, the plastic layer in Fig. 4B deformed permanently in both in-plane compression and wrinkling.

The central conclusions from Fig. 4 are twofold, both of which testify to the importance of yielding during release. First, at modest values of λ_{max} (Fig. 4A) the inelastic deformation of the plastic layer has a through-thickness gradient that is roughly uniform across the entire area of the sample. This causes it to stay bent even after debonding. The actual values of the permanent deformations also show a large degree of inelastic in-plane compression of the plastic during the release step. Second, at large values of λ_{max} (Fig. 4B), the wrinkles indicate that the inelastic deformation of the plastic has highly localized through-thickness gradients that are periodic along the X-direction. Such highly-localized inelastic bending is often called plastic hinge formation [34]. The formation of wrinkles allowed the plastic to maintain a large contour length, while conforming to the small length of the rubber at the interface.

3.1.2. Kinematics during release

While examination of the films after debonding gives insights into the final state after complete unloading, an examination of the videos during stretch and release offers further insights. The experiment with $\lambda_{max} = 3.1$ ($L = 18$ mm, $W = 8$ mm, $H^r = 750\ \mu\text{m}$) shown in Fig. 4B is considered again since it undergoes inelastic compression as well as inelastic wrinkling. For this experiment, two video cameras were used: a view normal to the Z-direction was used to quantify stretches, and a view at a shallow angle with respect to the X-Y plane was used to image wrinkle development. This latter video, entitled Video S1, is available as ESI, and the results are shown in Fig. 5.

Fig. 5A shows the evolution of reaction force with test time. Fig. 5B and C show the λ_x and λ_y calculated from the displacements of the markers applied on the specimen. The orange x-marks in the three graphs correspond to the three images in Fig. 5D–F. These images are portions of the sample at three times close to the instant when wrinkles are first evident in the video.

During the stretching phase, the force (Fig. 5A) and λ_x (Fig. 5B) both increase monotonically, whereas λ_y reduces (Fig. 5C). The black dashed curve in Fig. 5C corresponds to uniaxial kinematics, $\lambda_y = 1/\sqrt{\lambda_x}$, and is in excellent agreement with the measured λ_y.

The release step has two distinct phases. Up to a time of 335 s, the force reduces, and λ_x and λ_y approach 1. The measured λ_y remains consistent with uniaxial kinematics. Beyond 335 s (second

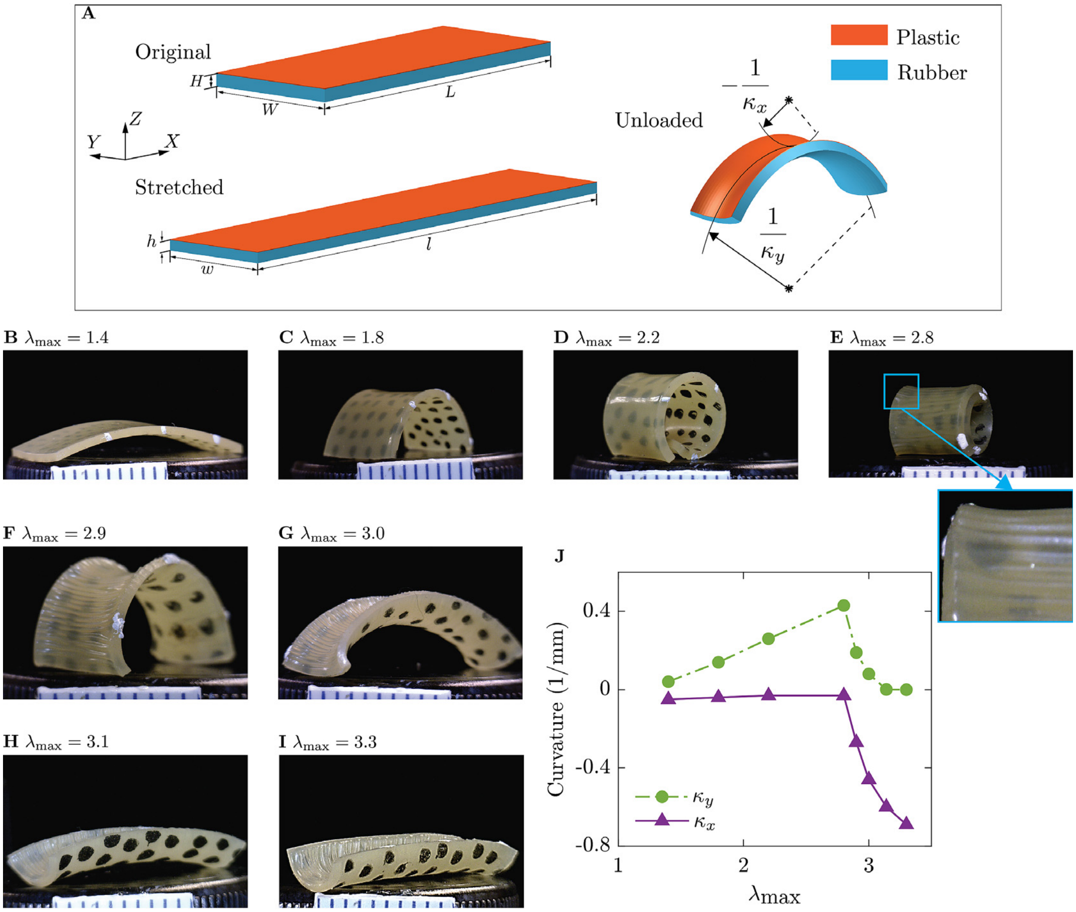

Fig. 3. (A) Schematic of a rectangular rubber-plastic bilayer specimen subjected to stretch of λ_{max} along X-direction. In general, the final morphology after unloading (right image) has two curvatures as indicated. The curvatures about the X and Y axes are denoted κ_x and κ_y where $\kappa_x < 0$ and $\kappa_y > 0$. The corresponding radii of curvature, $-\frac{1}{\kappa_x}$ and $\frac{1}{\kappa_y}$ are marked, where the * points indicate the centers around which the curvature develops. (B–I) Pictures of final shape for specimens as λ_{max} increases from 1.4 to 3.3. Spacing between the scale bar marking is 1 mm. Note the change in the direction and sign of the curvature between (E) and (H). Also note the wrinkles on the plastic face for E–I (J) Curvatures κ_x and κ_y vs λ_{max}.. (For interpretation of the references to color in this figure legend, the reader is referred to the web version of this article.)

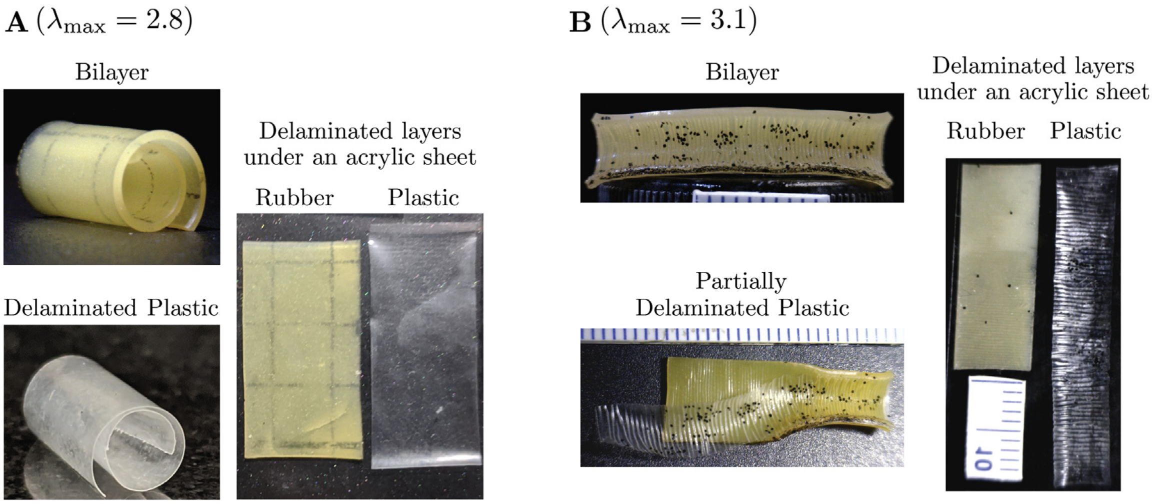

Fig. 4. (A) Roll shape is formed after stretching and unloading a rubber-plastic bilayer to $\lambda_{max} = 2.8$. The film keeps its shape when it is delaminated from the rubber substrate. (B) Half-tube shape is formed after unloading from $\lambda_{max} = 3.1$. Partially delaminated plastic shows permanent wrinkles. Thin white lines are apparent on the rubber indicating some local damage. Spacing between the scale bar marking is 1 mm.

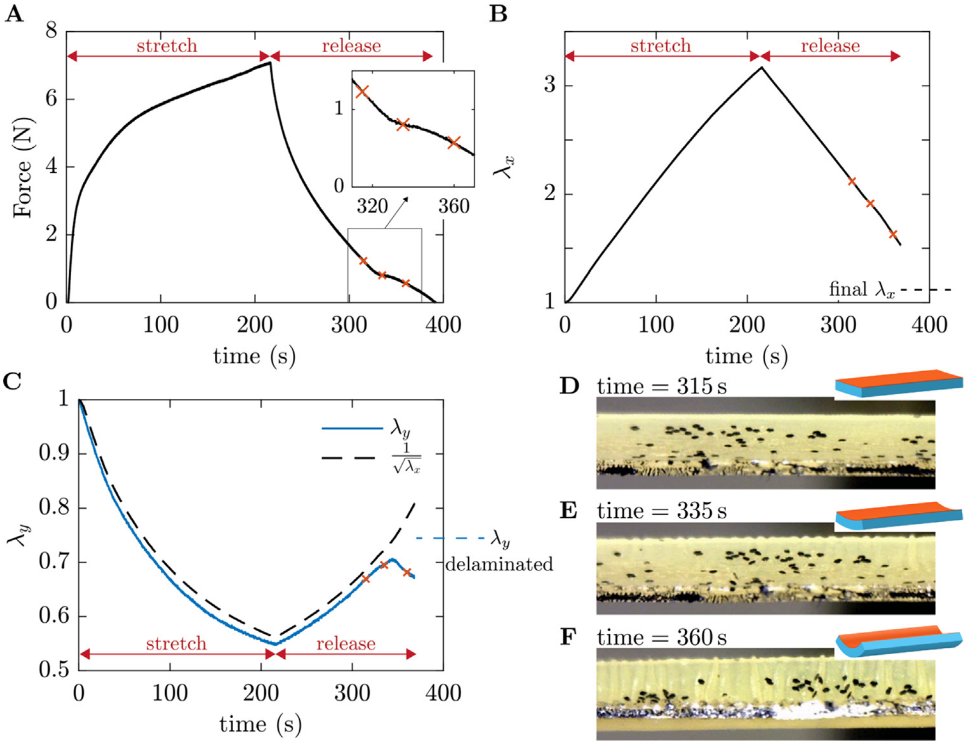

Fig. 5. Kinematics during loading and unloading of a 18 mm × 8 mm sample with $\lambda_{max} = 3.2$. (A) Reaction force with test time. (B) Stretch in the X-direction (λ_x) vs test time. Final λ_x from the fully-unloaded sample is shown as horizontal dashed line. (C) Stretch in the Y-direction (λ_y) vs test time. Final λ_y estimated from the width of the delaminated plastic layer is shown as dashed line. (D–F) Pictures of specimen at test times marked by orange x in A–C taken at an oblique angle (Inset shows schematic of sample shape). Wrinkles appear around time = 335 s. Specimen is strongly bent (i.e., $\kappa_x \neq 0$) in F.

orange x mark), several changes appear: there is an abrupt change in slope of the force vs time curve; the plastic face of the sample develops wrinkles (Fig. 5E); λ_y becomes smaller than expected from uniaxial kinematics; and the sample bends around the X-direction (Fig. 5F, but clearer in the corresponding video file Video S1). Due to this last effect, λ_y can no longer be estimated reliably from the DIC analysis of the video. These changes appear only in samples that wrinkle. Samples that do not wrinkle obey uniaxial kinematics throughout the release process and do not show any abrupt change in slope of the force–time curve.

The λ_x measured from the contour length of the fully-unloaded sample is shown as a horizontal dashed line in Fig. 5B. Further, the width of the plastic layer after delamination allows an estimate of the final value of λ_y in the fully-unloaded sample, and that value is shown as a dashed horizontal line in Fig. 5C. This final value of λ_y is below that expected from uniaxial kinematics.

The central insight from Fig. 5 is that wrinkles play a major role during the release step. The rubber seeks to reduce in length and increase in width during release, and it seeks to impose the same kinematics on the plastic. Prior to wrinkling, as the plastic layer is forced to reduce in length (λ_x decreases), it also increases in width (λ_y increases) consistent with uniaxial kinematics. Once wrinkles appear however, the plastic accommodates the x-direction compression by wrinkling, and the y-direction tension by bending, i.e., by developing κ_x. Accordingly, as judged from macroscopic shape changes, the width and length of the plastic layer appear to become decoupled: the length reduces continuously with time, whereas the width remains almost constant.

Yielding of the plastic, either with or without wrinkling, implies that the strain mismatch calculated from the permanent deformation of the free-standing layers does not determine the final shape. Accordingly, we now define "effective" strain mismatches $\overline{\lambda}_{x,mis}$ and $\overline{\lambda}_{y,mis}$, which are estimated from the permanent deformation of the delaminated layers. The horizontal dashed lines in Figs. 5B and 5C correspond to $\overline{\lambda}_{x,mis} \approx 1.1$, and $\overline{\lambda}_{y,mis} \approx 0.74$ respectively for this sample.

The same digital correlation analysis was repeated for all the samples and the effective strain mismatches were measured. They are shown against λ_{max} in Fig. 11C. The difference between Fig. 11A vs C quantifies the three effects of inelastic deformation. First, at all stretch values, $\overline{\lambda}_{x,mis} \ll \lambda_{x,mis}$ due to yielding during release. Second, for $\lambda_{max} \geq 2.8$ (exactly corresponding to the stretches at which wrinkles appear in Fig. 3), $\overline{\lambda}_{x,mis}$ reduces as λ_{max} increases. Such non-monotonic behavior of mismatch stretch could not have been anticipated from the behavior of the free-standing films at all. Finally, samples that wrinkle also deviate from uniaxial kinematics. This is shown by the small green circles which are the calculated values of $1/\sqrt{\overline{\lambda}_{x,mis}}$. The measured $\overline{\lambda}_{y,mis}$ remain close $1/\sqrt{\overline{\lambda}_{x,mis}}$ up to $\lambda_{max} < 2.8$ but are significantly smaller once wrinkles appear.

3.2. Effect of specimen width

The tests shown in Section 3.1 were repeated for specimens of width 2 mm, 4 mm, and 16 mm. In all cases, the undeformed length of the sample was kept at 18 mm and the rubber thickness was kept at 750 μm, same as in the previous section. The final shapes after applying λ_{max} of 1.8, 2.8, and 3.3 are shown in Fig. 6. For most samples, two images are shown, taken along the Y and X directions respectively to clearly indicate the two curvatures. The images in the 8 mm row are the same samples as in Fig. 3. The background colors of the table are chosen to distinguish between the various shapes: green for arch/roll shapes ($\kappa_y > 0$ and $\kappa_x \approx 0$), orange for saddles ($\kappa_y > 0$ and $\kappa_x < 0$), blue for tubular shapes ($\kappa_y \approx 0$ and $\kappa_x < 0$), and pink for helical ones.

The left column in Fig. 6 shows that at all widths, arches/rolls form at the smallest stretch examined. Width affects both, the

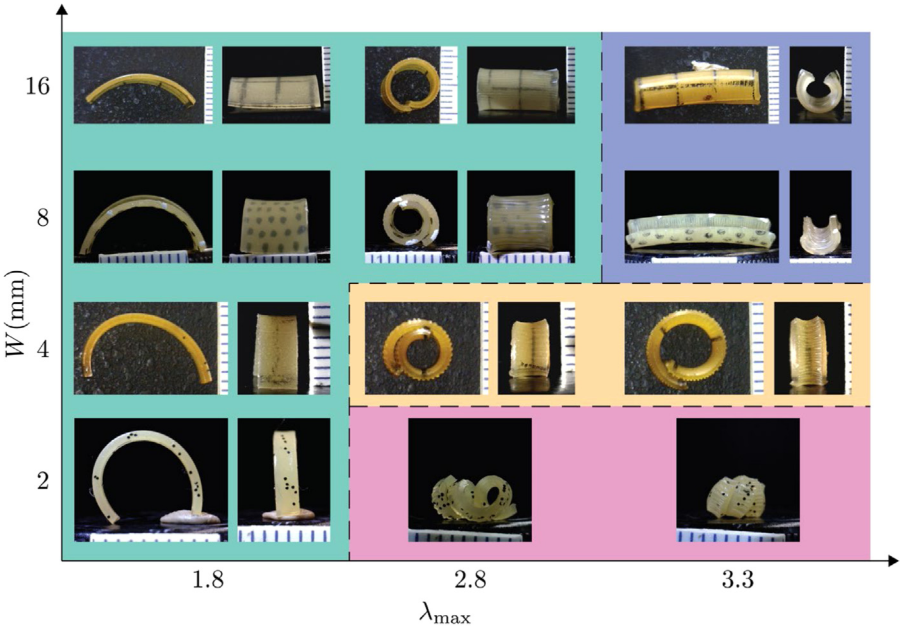

Fig. 6. The final shapes formed after stretching and unloading 2 mm, 4 mm, 8 mm, and 16 mm wide rubber-plastic bilayer specimens when λ_{max} is 1.8, 2.8, and 3.2. Two images, taken from orthogonal directions are shown for most samples. The 8 mm wide samples are the same as those discussed in Section 3.1. For the 2 mm wide sample, complex helical shapes appeared for large λ_{max} values. Spacing between the scale bar marking is 1 mm.

value of λ_{max} up to which arches are stable, and which shape appears at high stretch. As stretch increases, the narrowest samples transition into helices which will be discussed in Section 3.4. Wider samples first transition into saddles and then into half-tubes; increasing W raises the stretch needed for both transitions.

While Fig. 6 shows a transition from rolls to tubes directly at large W, Fig. 3 has already shown that for $W = 8$ mm, saddle shapes appear in between. Similar intermediate saddle shapes may exist at $W = 18$ mm as well. Further, at $W = 4$ mm, the magnitude of κ_y decreases, and that of κ_x increases as λ_x increases. I.e., even though unambiguous tubular shapes ($\kappa_y \approx 0$) are not evident up to the stretch examined, the trend is consistent with a saddle to tube transition.

3.3. Effect of rubber thickness

All the data thus far used a single rubber thickness of 750 μm. Fig. 7 shows the effect of reducing the rubber thickness using samples of the same lateral dimensions ($W = 8$ mm, $L = 18$ mm) as in Fig. 3. Reducing H^r has three distinct effects. First, the magnitude of curvature increases with decreasing rubber thickness. For example, the first column of Fig. 7 shows that for $\lambda_{max} = 1.8$, κ_y increases with decreasing rubber thickness. Second, when the rubber thickness is 500 or 250 μm, neither a saddle nor a tube shape is formed regardless of the λ_{max}. Instead, the final shapes are arch/roll when the λ_{max} is small, and more complex helical shapes when $\lambda_{max} = 3.3$. Although at first glance, these look distinctly different from the helices in Fig. 6, in fact, they show the same twisting deformations during release (see Section 3.4). Finally, wrinkles require significantly higher stretches to appear: the λ_{max} needed for wrinkles increases from 2.8 at $H^r = 750$ μm to 3.3 for $H^r = 500$ μm, whereas the bilayers with $H^r = 250$ μm do not show wrinkles at even the highest stretch examined.

3.4. Helical twisting

Apart from rolls, tubes, and saddles, rubber-plastic bilayers can form complex helical shapes. Helical shapes were also noted by Wisinger et al. [30]. Kanik et al. [13] also created helical springs in an elastic–plastic multilayer system, although the cross sections of their bilayers were not precisely rectangular. Figs. 6 and 7 show that twisting deformations are favored by narrow samples, thin samples, and by large stretch values prior to release.

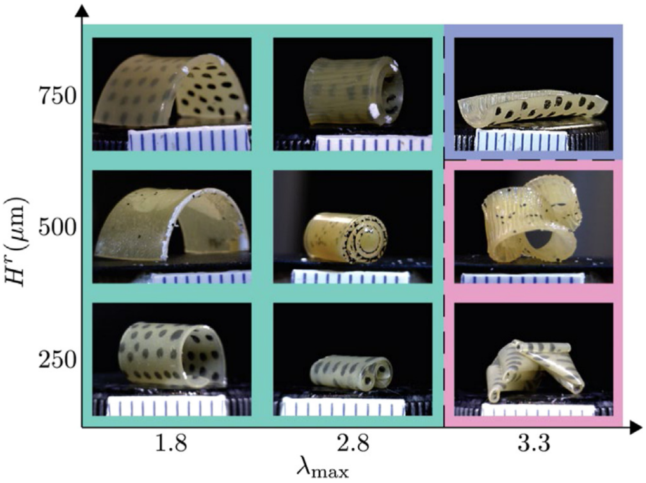

Fig. 7. The final shapes formed from bilayers with various rubber thicknesses. The samples with 250 μm and 500 μm thick rubber formed complex helical shapes when $\lambda_{max} = 3.3$. Spacing between the scale bar marking is 1 mm.

Insight into twisting deformations can be obtained from videos recorded during the unloading process (Video S2, Video S3), and snapshots from these videos are shown in Fig. 8. As the strain mismatch increases during release, the samples develop an internal stress that promotes bending around the Y direction; in an unconstrained sample, this would lead to $\kappa_y > 0$. However, during the release process, the sample is constrained by the grips, i.e., by a global tensile load. It appears therefore that the large out-of-plane twisting deformations permit bending with a $\kappa_y > 0$, even though the ends remain constrained. As the applied stretch reduces, the global tensile load reduces, thus allowing well-formed helices.

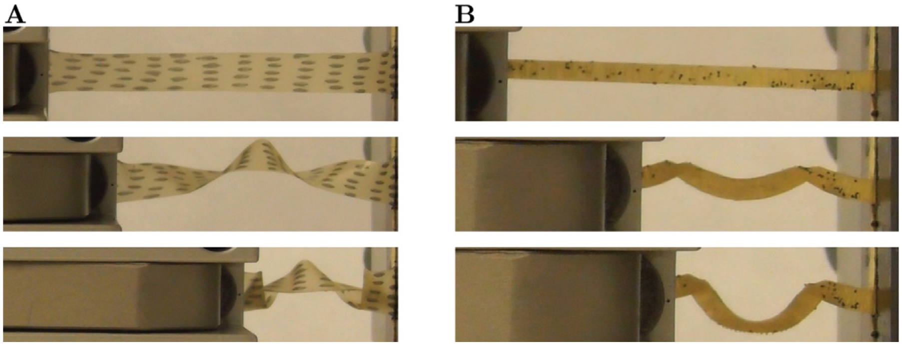

Fig. 8. Formation of helical shapes during release of samples with (A) 18 mm × 8 mm × 250 μm rubber and (B) 18 mm × 2 mm × 0.75 mm rubber.

It is interesting to note that in the two halves of the sample, the twist direction is opposite, because the grips not only impose an overall sample length, but also prohibit overall rotation. Thus, a vector drawn normal to a face of the sample cannot have net rotation around the *x*-direction. This induces the formation of mutually opposing twists, reconciled by a perversion near the middle of the sample [4,56–58]. In fact, experiments on elastic ribbons that have an intrinsic curvature (not shown) exhibit the same behavior during unloading suggesting that to a first approximation, such twisting is not due to inelastic deformation.

Yet, we note that after full unloading, the twisting deformation is permanent, i.e., despite the fact that the grips no longer constrain the sample, the helices cannot be induced to form rolls even by gentle manipulation by hand. Thus, some degree of inelastic deformation must be present which stabilizes the helical shapes.

3.5. Non uniform stretching

Section 2.2 mentioned that the LLDPE plastic did not show a peak in force displacement curve, and consistent with that, no necking was evident visually. However, many plastics, including many grades of polyethylene can undergo necking and subsequent drawing [59]. Previously [50,51] we discussed how necking and drawing can be regulated by bonding a rubber layer to a plastic. When the rubber layer is relatively thin, the deformation of the rubber-plastic bilayer resembles that of the necking plastic, albeit with a decrease in the stretch in the neck. Necking creates a non-uniform strain distribution, and thereby non-uniform elastic strain mismatch between layers. All the discussion in this paper presumed that the strain mismatch was uniform everywhere; here we briefly consider a counter example.

For studying the effect of non-uniform strain mismatch, bilayers were prepared by bonding LLDPE sheets of thickness $H^p = 120$ μm to styrene-ethylene/propylene-styrene (SEPS) rubber sheets of 50 μm thickness as previously reported [50]. Then 10 mm × 5 mm wide rectangular specimens were cut, subjected to an applied stretch of 2.5, and released.

Unlike the plastic film used in the earlier sections of this paper, the LLDPE used in this section shows strong necking under tension, and the onset of necking coincides with a peak in the force–displacement curve, shown in Fig. S2 in supplementary material. An image of a bilayer during stretching is shown in Fig. 9A. The non-homogeneous deformation is readily evident and quantified (see color map in Fig. 9A) using our previous procedure [50]. Upon unloading, from a relatively small stretch, the sample took on the shape in Fig. 9B, which resembles a hinge, i.e., substantially-flat regions connected by a sharply-bent region. If a larger displacement was imposed, the necked region showed localized twisting and resulted in the curled shape of Fig. 9C.

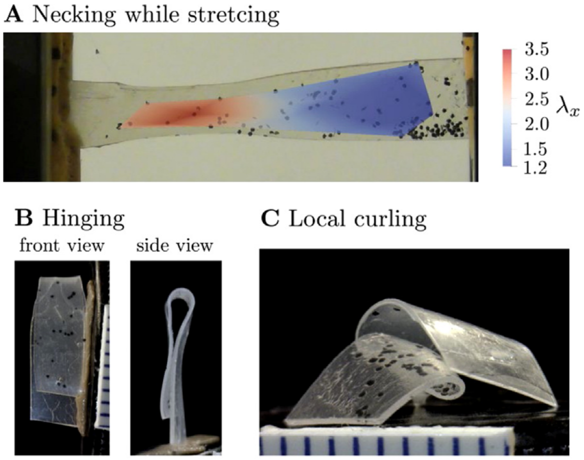

Fig. 9. (A) SEPS-LLDPE rubber-plastic bilayer specimen undergoing necking under stretching. Color map shows local stretch along the stretching direction. (B) Non uniform deformation creating a hinge. (C) Non uniform deformation creating a localized curling. Spacing between the scalebar marking is 1 mm.. (For interpretation of the references to color in this figure legend, the reader is referred to the web version of this article.)

Such localized necking may be exploited to realize strong localized bending, as common in origami design. The corresponding shape changes are however considerably complicated by the non-homogeneous strain distribution.

The central conclusion of this section therefore is that plastic materials are prone to necking under tension. Accordingly, when selecting materials for applications that exploit stretch-release behavior of elastic–plastic composites, it is crucial to know whether the free-standing plastic can neck or not.

4. Discussion: Strain-dependent arch to half-tube transition

In a bilayer with an elastic strain mismatch, unidirectional bending, saddle formation, wrinkling, and helical twisting all offer competing pathways for energy minimization. In fully-elastic bilayers, uniaxial elastic strain mismatch induces stable unidirectional bending [27]. Meanwhile, a equi-biaxial elastic strain mismatch creates dual curvature into bowl shapes at small mismatch, but bistable unidirectional bending into cylindrical shapes at large mismatch [60]. This paper shows that for elastic–plastic bilayers, uniaxial stretching and subsequent unloading induces formation of mono-stable arches/rolls, saddles, tubular shapes, or helical shapes. While formation of rolls and helix under uniaxial strain mismatch has been documented before [30] on a similar system, the formation of saddle and half-tube shapes through uniaxial loading is a new finding. To our knowledge, such a strain-dependent transition in the direction and sign of curvature has not been noted previously, and is the focus of this section.

Due to Poisson effects, uniaxial stretch-release creates non-equi-biaxial strain mismatch between the layers of the rubber-plastic bilayer such that $\epsilon_{x,mis} > 0$ and $\epsilon_{y,mis} < 0$. Here, ϵ is the logarithmic strain defined as $\epsilon = \ln(\lambda)$. A tube shape reduces ϵ_y while leaving ϵ_x unaffected, whereas a roll/arch shape reduces ϵ_x while leaving ϵ_y unaffected. Therefore when $\left|\epsilon_{y,mis}\right| > |\epsilon_{x,mis}|$, a tube is expected to be the favored configuration since it allows more energy reduction than a roll/arch shape. However, the magnitude of Poisson strain is much smaller than the imposed uniaxial strain ($\left|\epsilon_{y,mis}\right| < |\epsilon_{x,mis}|$.). Hence it is not clear how Poisson effects induce half-tube shapes or saddles when λ_{max} is large.

Section 3.1.2 showed that at large values of λ_{max} the elastic strain mismatch in the X and Y direction can become decoupled, coinciding with the formation of wrinkles. Therefore, in Section 4.1, through a minimal model we examine how the decoupling of elastic strain mismatch in the X and Y direction affect the shapes created. The model is not predictive, instead takes as input the final stretch at the interface in the X and Y direction.

4.1. Saddle model

As an approximation, the mechanical contribution of the plastic film is ignored. Accordingly, the plastic film is treated as a coating layer, without structural functionalities, which applies known strain mismatches $\lambda_{x,mis} > 1$ and $\lambda_{y,mis} < 1$, on the surface of the rubber sheet. Informed by the experimental observations, the rubber sheet is assumed to take on a saddle shape with a uniform curvature at all locations. The model identifies the combination of curvatures (κ_x, κ_y) that minimizes the total strain energy in the rubber. This approach is similar to [61]. Here (κ_x, κ_y) correspond to the curvatures of the centerlines of the top surface around the X and Y directions respectively. These saddles can approach arches/rolls ($|\kappa_x| \ll \left|\kappa_y\right|$) or half-tubes ($|\kappa_x| \gg \left|\kappa_y\right|$). Accordingly, the model can evaluate whether there is an arch to half-tube transition as the imposed stretches are varied. Any pairs of $\lambda_{x,mis}$ and $\lambda_{y,mis}$ can be imposed, including combinations that do or do not obey the uniaxial kinematic relationship, $\lambda_{y,mis} = 1/\sqrt{\lambda_{y,mis}}$. We emphasize that the mismatch stretches are not calculated from the model but provided as inputs from experimental measurements.

We represent the rubber as a neo-Hookean slab with dimensions L, W, and H^r in the reference configuration subjected to biaxial stretches $\lambda_{x,mis} > 1$ and $\lambda_{y,mis} < 1$ imposed on the top surface, which induce bending deformation (Fig. 10A). The corresponding strain energy density (ψ^r) is given by

$$\psi^r(\lambda_1, \lambda_2, \lambda_3) = \mu^r(\lambda_1^2 + \lambda_2^2 + \lambda_3^2 - 3) \tag{2}$$

where, μ_r is the shear modulus taken as 1 MPa, and λ_i ($i = 1$–3) are the principal stretches. Here 1 is taken as the X direction, 2 as the Y direction, and 3 as the Z direction (normal to the sample) in the undeformed reference configuration (Fig. 10A). Further, $\lambda_3 = \frac{1}{\lambda_1 \cdot \lambda_2}$, since volume is conserved.

The deformation gradient, $\boldsymbol{F}$, is decomposed multiplicatively into two parts, as the stretch mismatch, $\boldsymbol{F_m}$, and bending contribution, $\boldsymbol{F_b}$. The stretch mismatch is defined as follows:

$$\boldsymbol{F_m} = diag\left(\lambda_{x,mis}, \lambda_{y,mis}, \frac{1}{\lambda_1 \cdot \lambda_2}\right) \tag{3}$$

The bending contribution corresponds to a saddle shape, as in [61], namely:

$$\boldsymbol{F_b} = diag\left(\left(1 + \kappa_y z + (1 - \cos(-\kappa_x \cdot y))\left(-\kappa_y z - \frac{\kappa_y}{\kappa_x}\right)\right), (\kappa_x z + 1), \frac{1}{\lambda_1 \cdot \lambda_2}\right) \tag{4}$$

where z and y are the coordinates mapping points in the current configuration corresponding to the Z and Y ones in the reference configuration. We consider the following approximation: $z \in [0$ to $-h^r \approx \frac{H^r}{\lambda_{x,mis} \cdot \lambda_{y,mis}}]$, and $y \in [-\frac{w}{2} \approx -\frac{W \cdot \lambda_{y,mis}}{2}$ to $\frac{w}{2} \approx \frac{W \cdot \lambda_{y,mis}}{2}]$. The total deformation gradient is, $\boldsymbol{F} = \boldsymbol{F_b F_m}$:

$$\boldsymbol{F} = diag\left(\begin{array}{c} \left(\kappa_y z + \left(-\kappa_y z - \frac{\kappa_y}{\kappa_x}\right)(1 + \cos(y\kappa_x)) + 1\right)\lambda_{x,mis}, \\ (1 + \kappa_x z)\lambda_{y,mis}, \frac{1}{\lambda_1 \cdot \lambda_2} \end{array}\right) \tag{5}$$

Substituting these λ_i values into Eq. (2) then gives an explicit expression for ψ^r at any location within the slab. The total strain energy (U^r) in the rubber substrate is then evaluated by integrating the strain energy density ψ^r over the entire slab.

$$U^r = \int_{V^r} \psi^r dV \tag{6}$$

where V^r is the volume of the rubber slab. Given the slab dimensions and the mismatch stretches, we now seek the combination of curvatures, (κ_x, κ_y), that minimize U^r.

This minimization was conducted graphically as follows. A pair of curvatures (κ_x, κ_y) was selected. Eq. (2) (with λ_i values from Eq. (5)) was used to evaluate ψ^r (Eq. (2)) at all points on a 50×50 grid in the range $y \in [0, W]$ and $z \in [0, h^r]$. Integrating these values as per Eq. (6) gave the total strain energy U^r corresponding to the selected pair of curvatures. This calculation was repeated at all combinations of curvatures (κ_x, κ_y) within the range $\kappa_x h^r \in [0, 1)$ and $\kappa_y h^r \in [0, -1)$, with $\kappa_x h^r$ and $\kappa_y h^r$ increments of 0.02. This yielded the entire strain energy landscape $U^r(\kappa_x, \kappa_y)$, from which the curvatures corresponding to the minimum energy can be identified readily.

Fig. 10B is an illustrative plot of the dimensionless energy landscape, $U^r/\mu^r V^r$ against dimensionless curvatures $\kappa_x h^r$ and $\kappa_y h^r$ for $(\lambda_{x,mis}, \lambda_{y,mis}) = (1.4, 0.67)$, $W = 8$ mm and $H^r = 750$ μm. V^r is the volume of the rubber substrate. This pair of mismatch stretches show minimum energy for a saddle shape with nondimensional curvatures $\kappa_x h^r = -0.11$ and $\kappa_y h^r = 0.24$. The advantage of this graphical procedure is that it simultaneously confirms that for all cases in Fig. 11, U^r is convex shape with a single minimum, i.e., the predicted saddle shapes are stable.

The above procedure now allows us to predict the curvatures, and hence shape changes, corresponding to any prescribed ($\lambda_{x,mis}$, $\lambda_{y,mis}$). The chief question of interest is whether an arch to half-tube is predicted as increasing λ_{max} changes the values of ($\lambda_{x,mis}$, $\lambda_{y,mis}$).

We first apply the model, substituting the mismatch stretches from Fig. 11A, which were estimated from the free-standing films (Eq. (1)). Width is taken as 8 mm and thickness is 750 μm. It is important to note that these pairs of $\lambda_{x,mis}$ and $\lambda_{y,mis}$ obey uniaxial kinematics ($\lambda_{y,mis} = 1/\sqrt{\lambda_{x,mis}}$). The corresponding curvatures ($\kappa_x h^r$, $\kappa_y h^r$) that minimize strain energy U^r are shown in Fig. 11B. It is immediately apparent that in all cases, $\kappa_x \approx 0$, whereas $\kappa_y > 0$, i.e., only arch/roll shapes are predicted. This is in agreement with the existing literature [27].

Next, to capture the effect of inelastic compression and wrinkling, we apply the model using the mismatch stretches from

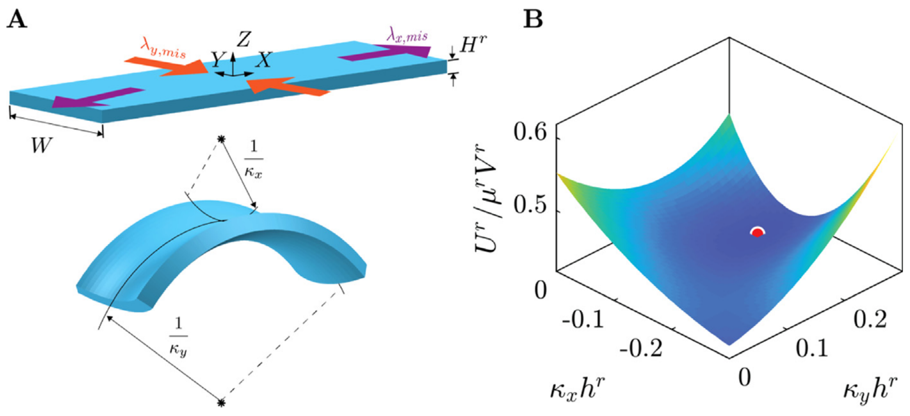

Fig. 10. (A) Illustration of boundary conditions on the model. The strain mismatches $\lambda_{x,mis}$ and $\lambda_{y,mis}$ are applied on the top surface. (B) Dimensionless energy landscape as a function of the two dimensionless curvatures $\kappa_x h^r$ and $\kappa_y h^r$.

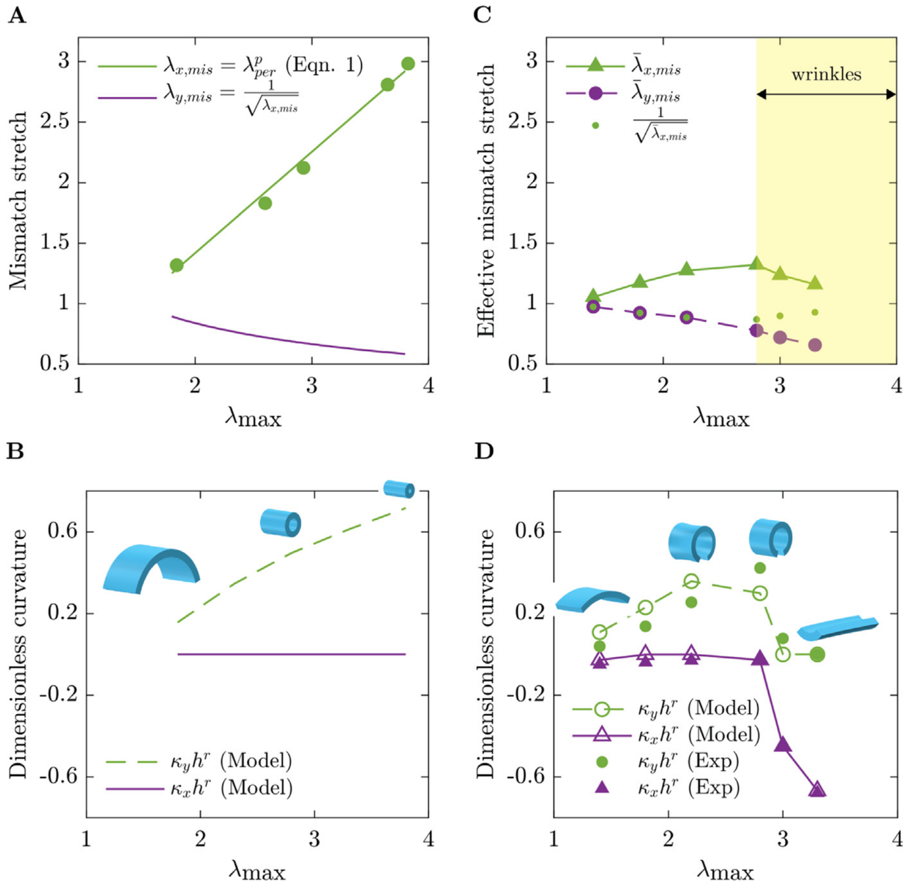

Fig. 11. (A) The mismatch stretches ($\lambda_{x,mis}$ *and* $\lambda_{y,mis}$) estimated from the behavior of the free-standing layers vs the maximum applied stretch. Here $\lambda_{x,mis}$ is taken to be equal to λ^p_{per}. (B) Model predictions for the normalized curvatures for the mismatch stretch from freestanding behavior of layers shown in Fig. 11A. (C) The effective strain mismatch obtained experimentally from the final configuration of bilayers shown in Fig. 3. (D) Model predictions for the normalized curvatures using the mismatch stretches from Fig. 11C. The experimentally measured dimensionless curvatures (same as from Fig. 3J) are shown as filled symbols.

Fig. 11C which were estimated from the final shape of the bilayers ($\bar{\lambda}_{x,mis}$, $\bar{\lambda}_{y,mis}$). As discussed in Section 3.1.2, these values are much smaller than those calculated from freestanding plastic due to inelastic deformation during the release step. Further, for samples that wrinkle (yellow shaded region in Fig. 11C), the X-direction mismatch reduces with increasing prestretch, and $\bar{\lambda}_{y,mis} \neq 1/\sqrt{\bar{\lambda}_{x,mis}}$. The corresponding curvatures that minimize the energy for the pairs ($\bar{\lambda}_{x,mis}$, $\bar{\lambda}_{y,mis}$) are shown in Fig. 11D. These trends are similar to those observed experimentally and do predict a transition from arch/roll shapes to tube shapes as the applied stretch increases. Indeed, even the quantitative values of the non-dimensional curvature are in excellent agreement with the measured values.

The central conclusion therefore is that a neo-Hookean slab of the geometry examined here, when subjected to biaxial surface stretches, does not show saddles shapes if the applied stretches obey uniaxial deformation kinematics. Surface stretch states that deviate from uniaxial kinematics may show saddle shapes. Furthermore, if $\lambda_{y,mis}$ is farther from 1 than expected from uniaxial kinematics, a curvature flip from an arch/roll to a tube is predicted that agrees quantitatively with experiments. Thus, at least for samples such as in this paper in which the plastic layer is thin, the central role of in-plane yielding and wrinkling is to decouple the mismatch stretches. The final shape can then be regarded as the response of the rubber slab to these stretches.

While the model is quantitatively successful in predicting curvatures and the transition in shapes with increasing λ_{max}, it has significant limitations. First, the strain energy in the film is ignored. Second, only three shapes are explored in the model, an arch/roll, tube, or a saddle. The model cannot capture helical deformations because of the kinematics considered. Third, the model is developed specifically for the cases examined here for which $L > W \gg H^r$, and the saddle shapes were presumed to be invariant along the X-direction. For samples with $L < W$ (not studied in this paper), the model is not suitable. Finally, and most importantly, the dependence of stretches $(\lambda_{x,mis}, \lambda_{y,mis})$ on λ_{max} is measured from experiments and is not solved for in the model. We reiterate that a full model including plasticity effects would be able to predict the mismatch stresses, and not provide them as input as done here.

5. Summary and conclusions

In summary, we have explored shape changes induced by stretching rectangular strips of rubber-plastic bilayer uniaxially, and then releasing them back to a stress-free state. Such shape changes result from deformation-induced strain mismatch: the plastic deforms permanently, whereas the rubber deforms elastically. Accordingly, upon stretching, the stress-free shape of the plastic is longer and narrower than of the rubber, and hence upon releasing, the specimen bends. We found that the bilayers formed helical shapes when the sample had small width or small thickness. Otherwise, the samples formed stable arch/rolls when the applied stretch was small, tubes when the applied stretch was large, and saddles when the applied stretch was intermediate. Perhaps the most unexpected result from this paper is that as the stretch prior to release is increased, the sign of curvature and direction of the curvature both flip: samples at small stretches bend into arches/rolls with the plastic on the outside, whereas at larger stretches, they bend into half-tubes with the plastic on the inside.

Much of this paper focuses on quantifying the role of inelastic deformation in the shape changes. We document numerous differences between elastic–plastic bilayers with a deformation-induced strain mismatch vs elastic–elastic bilayers with a strain mismatch induced by differential expansion or prestretching. Most importantly, we show that yielding of the plastic during release is a dominant feature of the mechanics of elastic–plastic bilayers. At small applied stretches, the rubber forces the plastic to yield in-plane. At large applied stretches, the plastic also yields by developing permanent wrinkles, and such wrinkling has an enormous effect on all aspects of shape changes. The net result of yielding is that the actual strain mismatch is far smaller than that expected from the behavior of free-standing plastic and rubber films. We have developed a model in which experimentally measured mismatch stretches act on the surface of a neo-Hookean slab, which then responds by bending into saddle shapes. In the limit of small or large stretches, these saddle shapes approach either arches or rolls, consistent with observations. While this model captures the curvature flip quantitatively, a full model that can predict the mismatch stretches remains to be developed. Overall, it appears that bending, twisting, saddle formation, in-plane yielding, and elastic or inelastic wrinkling are all competitive mechanisms that can relieve strain mismatch. Only a model that fully couples all these mechanisms can be truly predictive. Elastic–plastic composites are already being considered for applications such as artificial muscles, and further, deformation-induced strain mismatch can provide a new approach to origami design. A clear understanding of shape changes that come from an interplay of inelastic and elastic deformations can guide these new applications of elastic–plastic composites.

Declaration of competing interest

The authors declare that they have no known competing financial interests or personal relationships that could have appeared to influence the work reported in this paper.

Acknowledgments

This research was supported by the grant NSF-CMMI 1636064, NSF-2036164 and NSF-CMMI-1561789. We are grateful to Dr. Steven Abramowitch for the use of his tensile testing equipment.

L.D. gratefully acknowledges the partial support of the following grants: (i) The Italian MIUR with the “Departments of Excellence” Grant L. 232/2016, (ii) BOHME, FET EU grant No. 86317, (iii) PRIN 2017 20177TTP3S, (iv) FET Proactive (Neurofibres) grant No. 732344. L.D. also acknowledges the participation to the NIH, United States R56-HL142743-01 grant.

Appendix A. Supplementary data

Supplementary material related to this article can be found online at https://doi.org/10.1016/j.eml.2021.101384.

References

[1] S. Armon, et al., Geometry and mechanics in the opening of chiral seed pods, Science 333 (6050) (2011) 1726–1730.

[2] B. Li, et al., Surface wrinkling of mucosa induced by volumetric growth: Theory, simulation and experiment, J. Mech. Phys. Solids 59 (4) (2011) 758–774.

[3] C.M. Nelson, On buckling morphogenesis, J. Biomech. Eng. 138 (2) (2016) 021005.

[4] S.J. Gerbode, et al., How the cucumber tendril coils and overwinds, Science 337 (6098) (2012) 1087–1091.

[5] H. Liang, L. Mahadevan, The shape of a long leaf, Proc. Natl. Acad. Sci. USA 106 (52) (2009) 22049–22054.

[6] E. Katifori, et al., Foldable structures and the natural design of pollen grains, Proc. Natl. Acad. Sci. USA 107 (17) (2010) 7635–7639.

[7] E. Sharon, E. Efrati, The mechanics of non-Euclidean plates, Soft Matter 6 (22) (2010).

[8] T. Savin, et al., On the growth and form of the gut, Nature 476 (7358) (2011) 57–62.

[9] Y. Klein, E. Efrati, E. Sharon, Shaping of elastic sheets by prescription of non-Euclidean metrics, Science 315 (5815) (2007) 1116–1120.

[10] L. Ionov, Soft microorigami: Self-folding polymer films, Soft Matter 7 (15) (2011) 6786–6791.

[11] J. Kim, et al., Reversible self-bending soft hydrogel microstructures with mechanically optimized designs, Chem. Eng. J. 321 (2017) 384–393.

[12] E. Smela, et al., Electrochemical muscles - micromachining fingers and corkscrews, Adv. Mater. 5 (9) (1993) 630–632.

[13] M. Kanik, et al., Strain-programmable fiber-based artificial muscle, Science 365 (6449) (2019) 145–150.

[14] T.G. Leong, et al., Thin film stress driven self-folding of microstructured containers, Small 4 (10) (2008) 1605–1609.

[15] M. Huang, et al., Nanomechanical architecture of semiconductor nanomembranes, Nanoscale 3 (1) (2011) 96–120.

[16] W. Li, et al., Fabrication and stimuli-responsive behavior of flexible micro-scrolls, Soft Matter 8 (27) (2012).

[17] E. Smela, O. Inganas, I. Lundstrom, Controlled folding of micrometer-size structures, Science 268 (5218) (1995) 1735–1738.

[18] Z. Chen, et al., Tunable helical ribbons, Appl. Phys. Lett. 98 (1) (2011).

[19] D.P. Holmes, et al., Bending and twisting of soft materials by non-homogenous swelling, Soft Matter 7 (11) (2011) 5188–5193.

[20] T. van Manen, S. Janbaz, A.A. Zadpoor, Programming the shape-shifting of flat soft matter, Mater. Today 21 (2) (2018) 144–163.

[21] D.P. Holmes, Elasticity and stability of shape-shifting structures, Curr. Opin. Colloid Interface Sci. 40 (2019) 118–137.

[22] J. Geng, J.V. Selinger, Deformation of an asymmetric thin film, Phys. Rev. E (3) 86 (3 Pt 2) (2012) 036602.
[23] Z.A. Zhao, et al., Hydrophilic/hydrophobic composite shape-shifting structures, ACS Appl. Mater. Interfaces 10 (23) (2018) 19932–19939.
[24] Z. Hu, X. Zhang, Y. Li, Synthesis and application of modulated polymer gels, Science 269 (5223) (1995) 525–527.
[25] J.X. Cui, J.G.M. Adams, Y. Zhu, Controlled bending and folding of a bilayer structure consisting of a thin stiff film and a heat shrinkable polymer sheet, Smart Mater. Struct. 27 (5) (2018).
[26] N.A. Caruso, et al., Spontaneous morphing of equibiaxially pre-stretched elastic bilayers: The role of sample geometry, Int. J. Mech. Sci. 149 (2018) 481–486.
[27] A. DeSimone, Spontaneous bending of pre-stretched bilayers, Meccanica 53 (3) (2018) 511–518.
[28] J.M. Robertson, et al., Mechanically programmed shape change in laminated elastomeric composites, Soft Matter 11 (28) (2015) 5754–5764.
[29] Z. Chen, et al., Nonlinear geometric effects in mechanical bistable morphing structures, Phys. Rev. Lett. 109 (11) (2012) 114302.
[30] C.E. Wisinger, L.A. Maynard, J.R. Barone, Bending, curling, and twisting in polymeric bilayers, Soft Matter 15 (22) (2019) 4541–4547.
[31] Y.L. Shen, S. Suresh, Elastoplastic deformation of multilayered materials during thermal cycling, J. Mater. Res. 10 (5) (1995) 1200–1215.
[32] M. Finot, S. Suresh, Small and large deformation of thick and thin-film multi-layers: Effects of layer geometry, plasticity and compositional gradients, J. Mech. Phys. Solids 44 (5) (1996) 683–721.
[33] Y. Hu, A. Hiltner, E. Baer, Buckling in elastomer/plastic/elastomer 3-layer films, Polym. Compos. 25 (6) (2004) 653–661.
[34] A. Takei, et al., High-aspect-ratio ridge structures induced by plastic deformation as a novel microfabrication technique, ACS Appl. Mater. Interfaces 8 (36) (2016) 24230–24237.
[35] K. Srinivasan, G. Subbarayan, T. Siegmund, Wrinkling on irreversibly deforming foundations, Thin Solid Films 520 (17) (2012) 5671–5682.
[36] J. Yang, et al., Stretching-induced wrinkling in plastic-rubber composites, Soft Matter 13 (4) (2017) 776–787.
[37] Y.J. Ma, et al., Wrinkling of a stiff thin film bonded to a pre-strained, compliant substrate with finite thickness, Proc. R. Soc. Lond. Ser. A Math. Phys. Eng. Sci. 472 (2192) (2016) 6.
[38] J. Lin, et al., Bistable structures with controllable wrinkled surface, Extreme Mech. Lett. 36 (2020).
[39] Z.Y. Huang, W. Hong, Z. Suo, Nonlinear analyses of wrinkles in a film bonded to a compliant substrate, J. Mech. Phys. Solids 53 (9) (2005) 2101–2118.
[40] J. Song, et al., Buckling of a stiff thin film on a compliant substrate in large deformation, Int. J. Solids Struct. 45 (10) (2008) 3107–3121.
[41] L.H. Jin, A. Takei, J.W. Hutchinson, Mechanics of wrinkle/ridge transitions in thin film/substrate systems, J. Mech. Phys. Solids 81 (2015) 22–40.
[42] A. Takei, et al., Ridge localizations and networks in thin films compressed by the incremental release of a large equi-biaxial pre-stretch in the substrate, Adv. Mater. 26 (24) (2014) 4061–4067.
[43] J. Yin, et al., Deterministic order in surface micro-topologies through sequential wrinkling, Adv. Mater. 24 (40) (2012) 5441–5446.
[44] Y. Forterre, et al., How the Venus flytrap snaps, Nature 433 (7024) (2005) 421–425.
[45] B. Charlot, et al., Bistable nanowire for micromechanical memory, J. Micromech. Microeng. 18 (4) (2008).
[46] Z. Zhang, et al., Bistable morphing composite structures: A review, Thin-Walled Struct. 142 (2019) 74–97.
[47] P. Cendula, et al., Directional roll-up of nanomembranes mediated by wrinkling, Nano Lett. 11 (1) (2011) 236–240.
[48] P. Cendula, et al., Experimental realization of coexisting states of rolled-up and wrinkled nanomembranes by strain and etching control, Nanoscale 6 (23) (2014) 14326–14335.
[49] A.S. Argon, The physics of deformation and fracture of polymers, in: The Physics of Deformation and Fracture of Polymers, Cambridge University Press, Cambridge, U. K., 2013, pp. 325–341.
[50] R.G. Ramachandran, et al., Necking and drawing of rubber-plastic bilayer laminates, Soft Matter 14 (24) (2018) 4977–4986.
[51] R.G. Ramachandran, S. Maiti, S.S. Velankar, Necking and drawing of rubber–plastic laminate composites: Finite element simulations and analytical model, J. Mech. Phys. Solids 142 (2020).
[52] T. Li, Z. Suo, Deformability of thin metal films on elastomer substrates, Int. J. Solids Struct. 43 (7–8) (2006) 2351–2363.
[53] N. Lu, et al., Metal films on polymer substrates stretched beyond 50%, Appl. Phys. Lett. 91 (22) (2007).
[54] M.A. Holland, et al., Instabilities of soft films on compliant substrates, J. Mech. Phys. Solids 98 (2017) 350–365.
[55] M. Ben Bettaieb, F. Abed-Meraim, Localized necking in elastomer-supported metal layers: Impact of kinematic hardening, Trans. ASME, J. Manuf. Sci. Eng. 139 (6) (2017) 10.
[56] D. Wang, et al., Generation of perversions in fibers with intrinsic curvature, J. Mech. Phys. Solids 139 (2020).
[57] A. Goriely, M. Tabor, Spontaneous helix hand reversal and tendril perversion in climbing plants, Phys. Rev. Lett. 80 (7) (1998) 1564–1567.
[58] P. Pieranski, J. Baranska, A. Skjeltorp, Tendril perversion—A physical implication of the topological conservation law, Eur. J. Phys. 25 (5) (2004) 613–621.
[59] I.M. Ward, Mechanical properties of solid polymers, in: Mechanical Behavior of Solid Polymers, J. W Arrowsmith Ltd, Bristol, 1971, pp. 321–394.
[60] S. Alben, B. Balakrisnan, E. Smela, Edge effects determine the direction of bilayer bending, Nano Lett. 11 (6) (2011) 2280–2285.
[61] J. Wissman, et al., Saddle-like deformation in a dielectric elastomer actuator embedded with liquid-phase gallium-indium electrodes, J. Appl. Phys. 116 (14) (2014).